

Chapter 2

Recent Trends in Bias Temperature Instability

B. Kaczer, T. Grasser, J. Franco, M. Toledano-Luque, J. Roussel, M. Cho, E. Simoen, and G. Groeseneken

Abstract The paradigm shifts occurring in the past few years in our understanding of BTI are reviewed. Among the most significant ones is the shift from perceiving NBTI in terms of the Reaction-Diffusion model to analyzing BTI with the tools originally developed for describing low-frequency noise. This includes the interpretation of the time, temperature, voltage, and duty cycle dependences of BTI. It is further demonstrated that a wealth of information about defect properties can be obtained from deeply-scaled devices, and that this information can allow projection of variability issues of future deeply downscaled CMOS devices. The chapter is concluded by showing the most promising technological solutions to alleviate both PBTI and NBTI.

1 Introduction

Among the critical reliability issues facing present and future deeply downscaled CMOS devices is the so-called Bias Temperature Instability (BTI). While BTI in nFET devices was generally ascribed to charge trapping in the high-k portion of the gate oxide, the interpretation of BTI in pFET devices still generates controversy [1–7]. This phenomenon in pFET devices has been previously described by diffusion of hydrogen from and back into substrate/gate oxide interface states [8]. The so-called Reaction–Diffusion model based on this assumption is still popular, especially in the design community [9], despite being inconsistent with some crucial observations [10].

In this chapter, the elementary definitions and experimental observations of BTI are first briefly reviewed. One of the most intriguing properties of BTI—the lack

B. Kaczer (✉) • J. Franco • M. Toledano-Luque • J. Roussel • M. Cho
• E. Simoen • G. Groeseneken
imec, Leuven, Belgium
e-mail: kaczer@imec.be

T. Grasser
TU Wien, Wien, Austria

G. Groeseneken
KU, Leuven, Belgium

of characteristic time scale, especially in pFETs—is then argued to point to a *dispersion* in the underlying mechanism [5, 7, 11]. In CMOS technologies, a response on many time scales is typical for low-frequency noise [and its manifestation as Random Telegraph Noise (RTN) in deeply-scaled devices], suggesting that (the principal component of) BTI is in fact caused by the same defects [12, 13]. The link between BTI and low-frequency noise is then further developed—it is shown that many properties of gate oxide defects can be directly extracted from BTI relaxation measurements in deeply-scaled devices [14] and the noise-inspired model capable to fully describe these properties is reviewed. Afterwards it is shown how the understanding of gate oxide defect properties can be used to explain variability of BTI in deeply-scaled technologies, as well as possible technological solutions for both nFETs and pFETs.

2 Brief Overview of BTI

BTI is a consequence of charging of defect states in the gate oxide and at its interface [2]. The defects could be both pre-existing or generated during device operation. The trapped charge results in a shift of the device parameters, such as its threshold voltage V_{th} , channel mobility, transconductance, and subthreshold slope, and generally a decrease of the FET’s drive current. The name is derived from the phenomenon being strongly accelerated by *temperature* T and *gate bias* V_G . BTI in n-channel FET devices, which are typically biased in circuits at positive V_G , is referred to as Positive BTI (PBTI), while negative BTI (NBTI) takes place in p-channel FETs. Constant V_G stress bias is often referred to as static, or “DC” BTI, while periodically interrupted V_G stress is called “AC”, or dynamic BTI.

3 Static BTI

Figure 2.1 illustrates the typical gradual shift of pFET threshold voltage ΔV_{th} during accelerated stress at elevated T [5]. The stress data are typically measured at several V_G ’s and ΔV_{th} is extrapolated to 10 years at the circuit operating voltage V_{DD} (or $V_{DD} + 10\%$). The extrapolated ΔV_{th} must be below a given value (typically 30 or 50 mV) for the technology to qualify.

This simple extrapolation procedure is, however, complicated by ΔV_{th} decreasing *immediately* after the stress bias is removed, as illustrated in Fig. 2.1 [15]. As will be discussed henceforth, this *recovery*, or *relaxation*, component R typically proceeds simultaneously on many time scales, making it difficult to determine its beginning or end and thus separating it from the final *non-recoverable*, or *permanent*, component P [2, 6]. This ΔV_{th} relaxation is thus a crucial problem for BTI measurement, interpretation, and extrapolation.

Fig. 2.1 Shift in pFET threshold voltage is observed during negative gate bias stress. When the stress bias is removed, a recovery of the effect is seen (note: $V_{th} \sim 0$ V for this device). Inset illustrates the biases applied at FET terminals during the BTI measurement

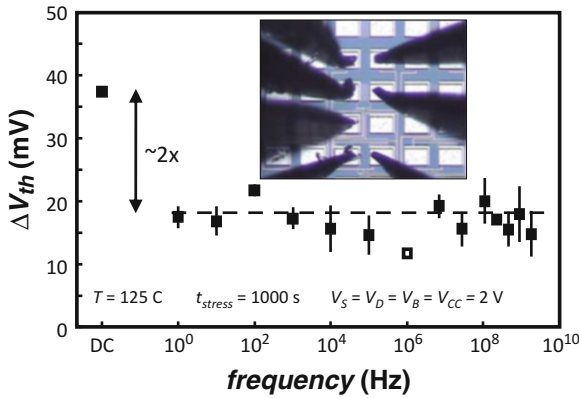
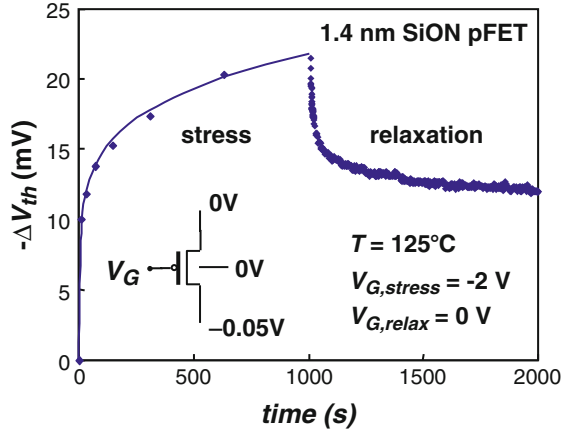
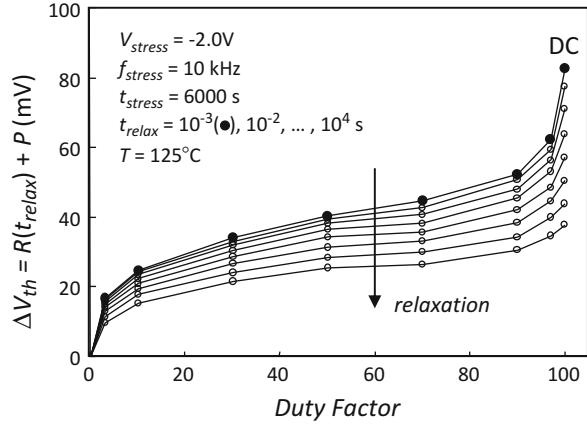


Fig. 2.2 The V_{th} shifts due to 50 % AC unipolar NBTI stress in pFETs are seen independent of frequency in the entire frequency range of 1 Hz–2 GHz. The V_{th} shift of the corresponding DC NBTI stress obtained on an identical device is shown for comparison. Inset: Micrograph of the *on-chip* circuit for the DC and AC BTI measurements consisting of a ring oscillator, a frequency divider, a buffer, a pass-gate-based multiplexer, and the device under test [17]

4 Dynamic BTI

In many CMOS applications, such as logic, the majority of the FETs are constantly switched and thus exposed to *dynamic* stress [16]. Figure 2.2 documents that NBTI is present at frequencies up to the GHz range, i.e., there does not appear to be any “cut-off” time constant of the degradation mechanism above ~ 1 ns [17]. Furthermore, the AC bias signal reduces BTI with respect to the DC stress. This provides some additional reliability margin, which can be factored in during the application design phase [9].

Fig. 2.3 Total degradation ΔV_{th} after 6000 s of unipolar NBTI stress shows a distinctive dependence on the duty factor DF . In particular, a weak dependence, or a “plateau” between ~ 10 and ~ 90 % is observed, complemented by rapid ΔV_{th} increase for the outermost DF values. Data at different relaxation times are shown



In an arbitrary FET of an arbitrary digital circuit, the average probability of a signal being high can vary between 0 and 100 %. The dependence of BTI on the *duty cycle* (called *duty factor* or DF here) thus needs to be studied. A NBTI ΔV_{th} - DF dependence with an inflection point around $DF \sim 50$ %, first reported in [17], is shown in Fig. 2.3 [12].

5 Similarity Between BTI Relaxation and Low-Frequency Noise

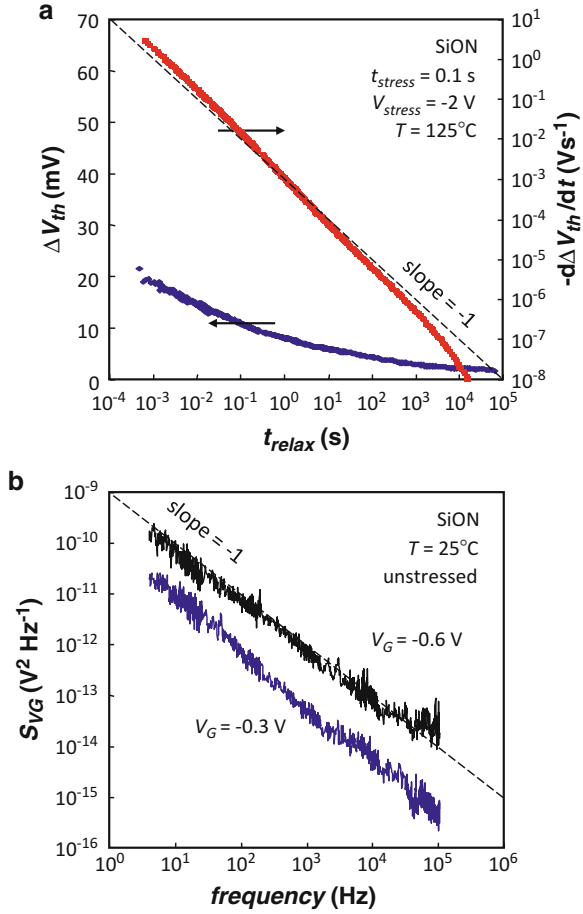
Long, $\log(t)$ -like behavior of ΔV_{th} without a characteristic time scale is typically observed in both the initial portion of NBTI degradation [13, 18] and the recovery phase. Figure 2.4 illustrates that the *rate of degradation* $d\Delta V_{th}/dt_{relax}$ [7] extracted from the $\log(t_{relax})$ -like ΔV_{th} NBTI relaxation transient after even a *very short*, 0.1 s stress, follows $1/t_{relax}$ for over seven decades. Such behavior is a signature of states with discharging time constants covering as many decades [19].

Incidentally, *superposition of states with widely distributed time scales* is the standard explanation of the $1/f$ noise spectra [20], which are clearly observed in our pFETs (Fig. 2.4). This obvious similarity leads us to argue that the same states with widely distributed time scales in fact play a fundamental role in both NBTI and noise measurements.

6 Semi-quantitative Model for BTI Relaxation

In order to visualize this common property it is beneficial to consider an equivalent circuit representing states with widely distributed time scales [19]. Note that in either NBTI relaxation or $1/f$ noise measurements, no maximum or minimum “cut-

Fig. 2.4 (a) A characteristic long, log-like ΔV_{th} relaxation trace is observed after even short (pulse-like) NBTI stress. The rate of recovery $d\Delta V_{th}/dt_{relax}$ following $\sim 1/t_{relax}$ for ~ 7 decades is a signature of states with discharging time constants covering as many decades. (b) Gate-referred noise spectra measured on the same (unstressed) devices show clear $1/f$ dependence, routinely explained by a superposition of states with widely distributed time scales



off” times are typically observed [12]. For the sake of simplicity it is therefore assumed here that the time constants are log-uniformly distributed from times much shorter than the switching time of a pFET to very long, corresponding to the lifetime of a CMOS application. Such states with widely distributed time scales are then represented by “RC” elements in Fig. 2.5 with the total FET ΔV_{th} being proportional to the sum of voltages (“occupancies”) on all capacitors. For the sake of simplicity, it is assumed that all RC elements have the same weight and can be partially occupied, which emulates the behavior of a large-area device. Most properties of the recoverable component can be reproduced when the ohmic resistors in Fig. 2.5 are replaced with a *non-linear* component (simulated by two diodes with different parameters, see Fig. 2.5), which emulates different charging (i.e., capture) and discharging (i.e., emission) time constants of each defect [21]. Such a circuit correctly reproduces DF (Fig. 2.6, cf. Fig. 2.3) and also the log-like relaxation (Fig. 2.4a) and the log-like initial phase of stress (not shown) [19].

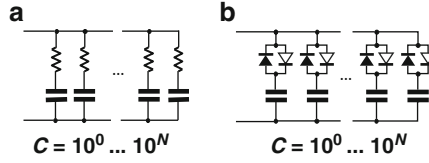
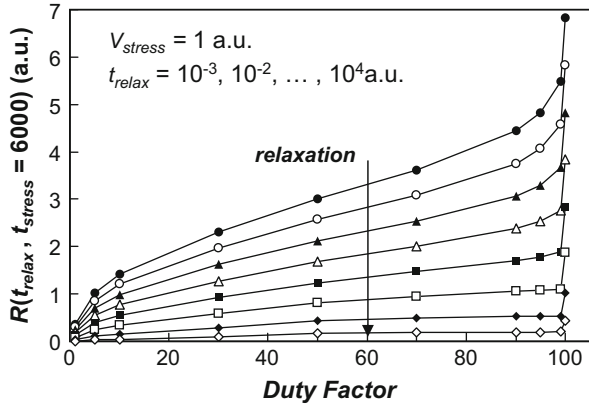


Fig. 2.5 (a) An equivalent circuit with exponentially increasing capacitances used to emulate defect states with widely distributed time scales, such as those active in low-frequency noise. (b) The same circuit modified to account for charging (i.e., capture) and discharging (i.e., emission) time constants being voltage dependent, represented by asymmetric diodes. The sum of voltages on capacitors is assumed to be proportional to FET ΔV_{th}

Fig. 2.6 The plateau in DF dependence of R is also qualitatively well reproduced by the equivalent circuit in Fig. 2.5, as is the decrease with increasing relaxation time (cf. Fig. 2.3, which, however, shows the sum of R and P)



7 Properties of Individual Defects

Figure 2.7 shows two typical ΔV_{th} relaxation transients following positive V_G stress on a single $70 \times 90 \text{ nm}^2$ nMOSFET (i.e., corresponding to PBTI). Conversely to the continuous relaxation curves obtained on large devices, a quantized ΔV_{th} transient is observed in the deeply-scaled devices. In such devices, the relaxation is observed to proceed in discrete voltage steps, with each step corresponding to discharging of a *single* oxide defect [12, 22, 23]. Upon repeated perturbation, each defect shows up in the relaxation trace with a characteristic “fingerprint” consisting of its discharge, or *emission* time, and its voltage step [14].

Figure 2.8 shows the two-dimensional histogram of the heights and the emission times of the steps when the experiment was repeated 70 times at the same stressing and relaxing condition as in Fig. 2.7 [14]. In Fig. 2.8, four clusters are clearly formed that correspond to four active defects in the time window of the experimental setup.

The emission times of each defect are stochastically distributed and follow an exponential distribution. This allows us to determine the average emission time τ_e . The capture time of each trap can be obtained by varying the stress (i.e., charging) time from 240 ms down to 2 ms. The intensity of the cluster decreases with reducing

Fig. 2.7 Characteristic ΔV_{th} transients of a single $70 \times 90 \text{ nm}^2$ $1 \text{ nm-SiO}_2/1.8 \text{ nm-HfSiO}$ nMOSFET device stressed at 25°C and $V_G = 2.8 \text{ V}$ for 184 ms . Four discrete drops are observed indicating the existence of four active traps at this stress condition

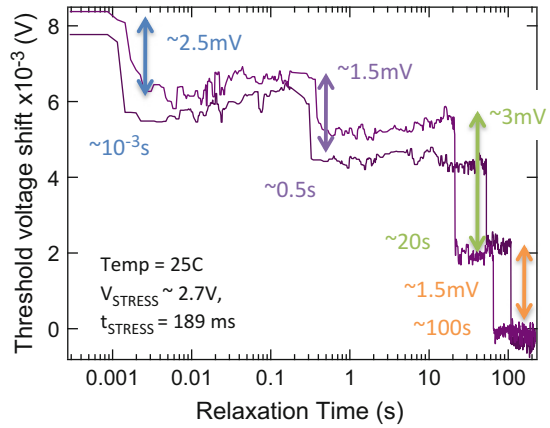
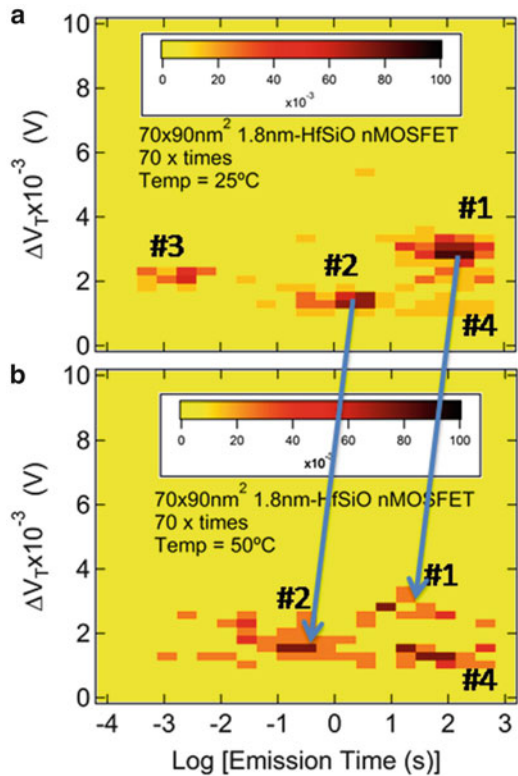


Fig. 2.8 Two-dimensional histograms (TDDS spectra) of the heights and emission times of the steps extracted from $70 \Delta V_{th}$ transients of the particular device of Fig. 2.7 at (a) 25°C and (b) 50°C . Four clusters are formed that shift horizontally to shorter emission times with increasing temperature. Note that trap #3 disappears from the experimental window at 50°C



stress time when the characteristic capture time is in the range of the stress time. The fit of the intensity to $P_c = 1 - \exp(-t_{stress}/\tau_c)$ lets us calculate the average capture time τ_c . This technique is known as Time Dependent Defect Spectroscopy (TDDS) [14].

In Fig. 2.8, an identical experiment was repeated at 50 °C on the same device. Note the large horizontal shift of the clusters to shorter emission times with only a 25 °C temperature increase. The Arrhenius plots of the emission and capture times obtained at T from 10 to 50 °C (not shown) provide activation energies of 0.48 eV for emission and 0.25 eV for capture. Similarly thermally activated capture and emission times are also observed in both nFET and pFET (i.e., corresponding to NBTI) with conventional SiO₂ gate oxide [14, 23, 24]. One can therefore conclude for all these cases that *both emission and capture in both electron and hole gate oxide traps are without a doubt thermally activated processes*. This experimental fact is incompatible with direct elastic tunneling theories widely used in different oxide trap characterization techniques and calculations. Consequently, a new model that takes into account this thermal dependence has to be considered.

8 Modeling Properties of Individual Defects

A model of the above-described properties of individual gate oxide defects can be constructed by drawing on the above similarities with low-frequency and Random Telegraph Noise (RTN) [25]. An example of the configuration coordinate diagram of the model is shown in the inset of Fig. 2.9. Four different configurations of the defect are considered [14]. Two of the states are electrically neutral while two of them correspond to the singly positively charged state. In each charge state the defect is represented by a double well, with the first of the two states being the equilibrium state and the other a secondary (metastable) minimum. The time dynamics of the defect can be described by a simple stochastic Markov process. Broadly, transition rates between states involving charge transfer assume (1) tunneling between the substrate and the defect, and (2) nonradiative multiphonon (NMP) theory, which has been often applied to explain RTN [26, 27]. Introduction of the NMP theory naturally explains the temperature dependence of both capture and emission time constants observed in the previous section. The wide distribution of time scales is then readily described by a distribution of the overlaps of the potential wells (i.e., a distribution of “potential barriers”) [14].

The crucial extension of the NMP theory is the assumption of the relative position of the potential wells changing with gate bias [14], quite naturally introducing the required strong V_G dependence. As documented in Fig. 2.9, the model successfully describes the bias as well as the temperature dependences of the characteristic time constants. It is also noted that, contrary to techniques for the analysis of RTN, which only allow monitoring the defect behavior in a rather narrow time window, TDDS can be used to study the defects capture and emission times over an extremely wide range.

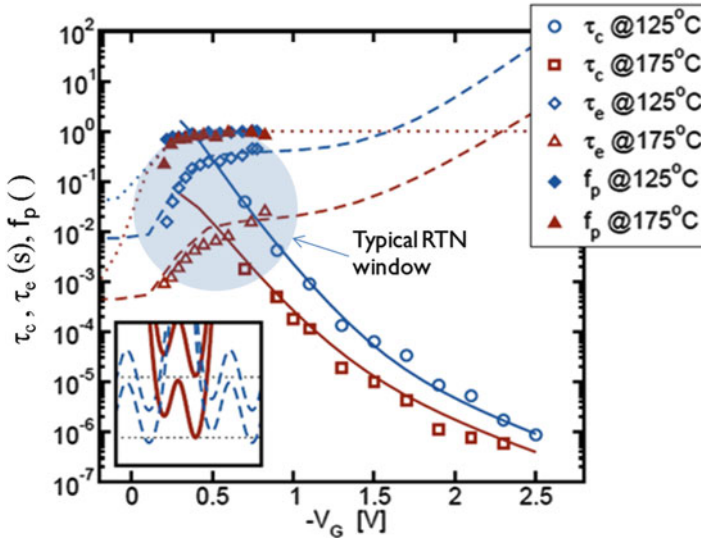


Fig. 2.9 Simulated capture and emission time constants (*lines*) compared with to the experimental TDDS values obtained on SiO₂ pFETs (*symbols*) during NBTI stressing at 125 and 175 °C and varying V_G . The experimental occupation probability of the charged state f_p is also indicated. The configuration coordinate diagram is shown in the inset (*dashed line*: neutral defect state; *solid line*: charged state potential)

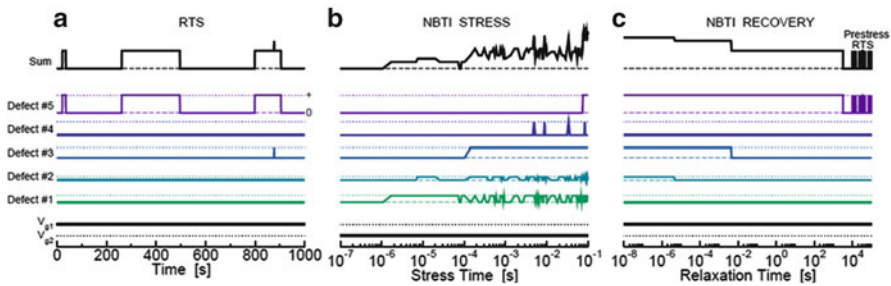
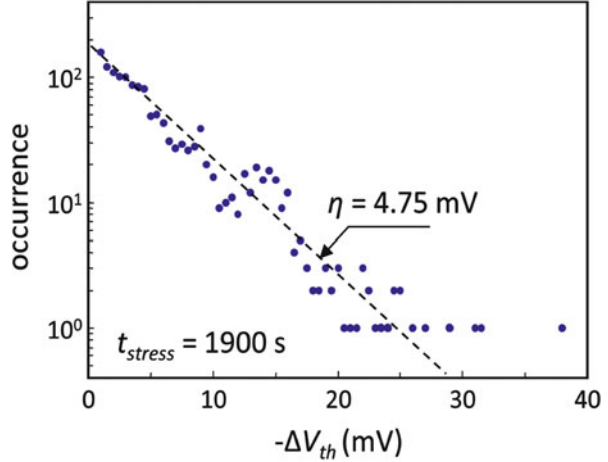


Fig. 2.10 Simulated RTN, stress, and recovery behavior of a nano-scale device using a stochastic solution algorithm of the proposed model. (a) At the threshold voltage (V_{G1}), the RTN is dominated by defect #5 with the occasional contribution from defect #3. Defects #1, #2, and #4 remain positively charged within the ‘simulation/experimental’ window. (b) During stress (V_{G2}), the capture times are dramatically reduced by the higher (more negative) gate voltage and the defects #3 and #5 become predominantly positively charged ($\tau_c \ll \tau_e$). Defects #1, #2, and #4 start producing RTN. (c) During recovery (back at V_{G1}), trapped charge is subsequently lost and the dynamic equilibrium behavior is gradually restored

It has been previously argued that the phenomenon called NBTI relaxation in pFET devices is in fact just a different facet of the well-known low-frequency noise in these devices. While the low-frequency noise corresponds to the channel/gate dielectrics system being in the state of dynamic equilibrium, NBTI relaxation corresponds to the perturbed system returning to this equilibrium [28]. Figure 2.10

Fig. 2.11 Histogram of NBTI transient individual step heights measured on 72 devices shows a clear exponential distribution. The average V_{th} shift η corresponding to a single carrier discharge is 4.75 ± 0.30 mV in the pFETs with metallurgic length $L = 35$ nm, width $W = 90$ nm, and HfO_2 dielectrics with $\text{EOT} = 0.8$ nm



then illustrates this concept on a simulated example of a deeply scaled pFET containing only five active defects [23]. In particular it shows that the same defects can be responsible both for RTN as well as the NBTI relaxation and the (initial phase of) NBTI stress.

9 BTI Distribution in Deeply-Scaled FETs

As CMOS devices scale toward atomic dimensions, device parameters become statistically distributed. Similarly, parameter *shifts* during device operation, once studied in terms of the average value only, will have to be described in terms of their distribution functions. The understanding of the properties of individual defects helps us to explain this distribution. Namely, much like in the case of random telegraph noise (RTN) [29, 30], it is observed the distribution of down-steps ΔV_{th} due to *individual* discharging events to be *exponentially* distributed (Fig. 2.11). The exponential distribution of single-charge ΔV_{th} can be understood if non-uniformities in the pFET channel due to random dopant fluctuations (RDF) are considered [28–30]. A *single* discharging event in many devices routinely exceeded 15 mV, and in several devices exceeded 30 mV, the NBTI lifetime criterion presently used by some groups. For comparison, ΔV_{th} of less than 2 mV would be expected based on a simple charge sheet approximation. The large observed step height amplitude is due to the aggressively scaled dimensions of the pFETs used [28, 31].

Assuming the lateral locations of the trapped charges are uncorrelated, the overall ΔV_{th} distribution can be readily expressed as a convolution of individual exponential distributions [28, 31]. An actual population of stressed devices will

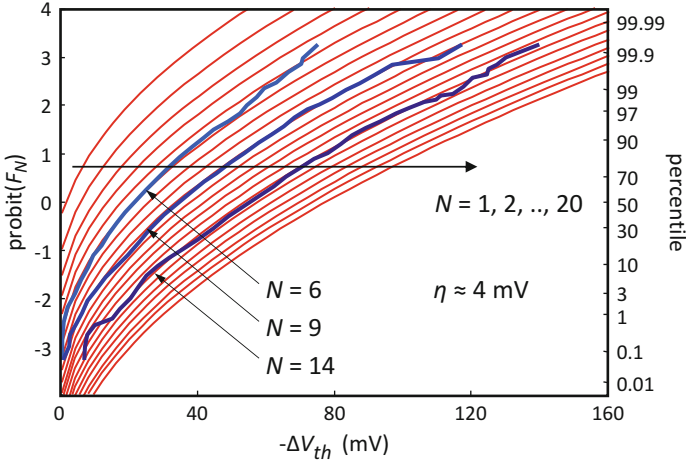


Fig. 2.12 Equation (2.1) in a probit plot rescaled to fit experimental distributions from Fig. 2.10 of Ref. [22], with the corresponding values of N and η readily extracted

consist of devices with a *different* number n of oxide defects in each device, with n being Poisson distributed [12, 22, 28]. The *total* ΔV_{th} distribution can be therefore obtained as

$$F_N(\Delta V_{th}, \eta) = \sum_{n=0}^{\infty} \frac{e^{-N} N^n}{n!} \left[1 - \frac{n \Gamma(n, \Delta V_{th}/n)}{n!} \right], \quad (2.1)$$

where N is the mean number of defects in the FET gate oxide and is related to the oxide trap (surface) density N_{ot} as $N = W L N_{ot}$. The CDF is plotted in Fig. 2.12 for several values of N . For comparison, measured total ΔV_{th} distributions for three different stress times from Ref. [22] are excellently fitted by the derived analytical description.

The advantage of describing the total ΔV_{th} distribution in terms of Eq. (2.1) is its relative simplicity and tangibility of the variables. The analytical description allows, among other things, to calculate NBTI threshold voltage shifts in an unlimited population of devices, a feat practically impossible through device simulations.

10 Technological Solutions

Once the underlying BTI mechanisms are understood, the defect properties can be modified to beneficial ends. Below, two possible technological solutions for both PBTI and NBTI are discussed.

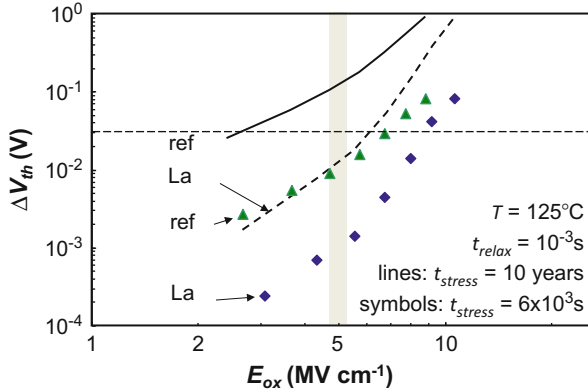


Fig. 2.13 A significant reduction of PBTI threshold voltage shift is observed in planar nFETs with La passivation (“La”) over the reference stack (“ref”) without passivation. Simplified power-law projection to 10 years shows passivated stack having sufficient reliability ($\Delta V_{th} < 30$ mV) at ~ 5 MV/cm operating field

11 Improving PBTI with Rare-Earth Incorporation

PBTI was considered a minor problem in technologies based on SiO_2 . It arose as a reliability issue when high- k materials were incorporated into the gate stack. However, when rare earths were introduced to adjust the nFET initial threshold voltage, this issue was mitigated, as can be seen in Fig. 2.13. A significant reduction of PBTI is observed in planar nFETs with lanthanum with respect to a lanthanum-free reference [32].

Positive BTI in nFETs with high- k materials like HfO_2 has been linked to oxygen vacancies, which produce a defect level in the upper part of the oxide band gap. Group III elements compensate unpaired electrons around the oxygen vacancy in HfO_2 and the defects are “passivated” by being pushed up toward the conduction band minimum [33]. Such states are not easily accessible to nFET channel electrons, resulting in the significant reduction of negative charge capture in the stack and hence the reduction of PBTI.

12 Improving NBTI in High-Mobility SiGe pFETs

Reduction of gate stack EOT, which is one of the most efficient ways to improve FET performance, enhances NBTI due to increased oxide electric field. As a consequence, 10 year lifetime can be guaranteed for sub-1 nm EOT Si pFETs only at gate overdrive voltages far below the expected operating voltages (Fig. 2.14).

Another way to improve FET performance is the use of high-mobility substrates, such as buried-channel SiGe [34]. Because of the valence band offset between the

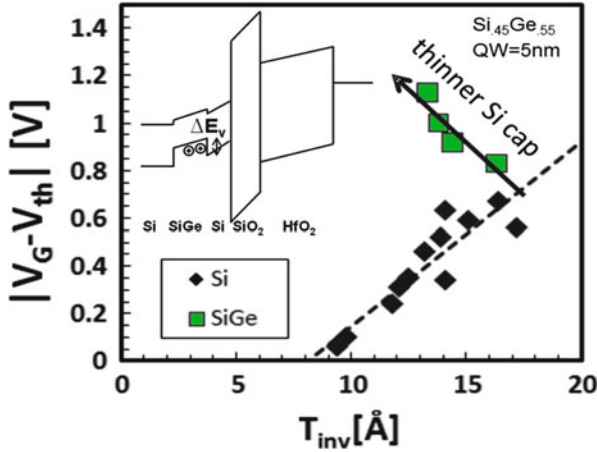


Fig. 2.14 Plot of the operating overdrive voltage $|V_G - V_{th}|$ for 10 year lifetime assuming a 30 mV threshold voltage shift criterion vs. the inversion capacitance equivalent thickness T_{inv} , for Si channel devices with different processing used as a reference, and for SiGe pFETs. For low T_{inv} , Si devices $|V_G - V_{th}|$ is below the expected operating voltage. In contrast to that, optimized SiGe devices show improved lifetime. *Inset*: gate-stack band diagram in inversion. Si cap acts as a barrier ΔE_V for holes

SiGe and the Si cap (see inset of Fig. 2.14), inversion channel holes are confined in the SiGe layer, which therefore acts as a quantum well (QW) for holes. The Si cap lowers the inversion capacitance as compared to the accumulation capacitance. For these devices it is therefore necessary to report the capacitance-equivalent thickness in inversion (T_{inv} , evaluated at $V_G = V_{th} - 0.6$ V) which will be affected by the thickness of the Si cap [35].

As can be seen from Fig. 2.14, SiGe-based device gate stacks significantly increase operating gate overdrive while still guaranteeing 10 year device lifetime and at the moment seem to be the only solution to the NBTI issue for sub-1 nm EOT devices. It has been recently observed that both increasing the Ge content in the channel as well as increasing the SiGe QW thickness reduces NBTI. Most intriguingly, a *reduction* of Si cap thickness also diminishes NBTI [35]. The most likely hypothesis explaining all three trends appears to be the energetic decoupling of the buried channel and the gate oxide defects [36].

Conclusions

In this chapter some of the shifts occurring in the past few years in our understanding of BTI were reviewed. Among the most significant ones is the shift from perceiving NBTI in terms of the Reaction–Diffusion model to analyzing BTI with the tools originally developed for describing low-frequency

(continued)

noise. This includes the interpretation of the time, temperature, voltage, and duty cycle dependences of BTI. It was further demonstrated that a wealth of information about defect properties can be obtained from deeply-scaled devices, and that this information can allow interpretation of variability issues of future deeply downscaled CMOS devices. This theme was complemented by showing the most promising technological solutions to alleviate both PBTI and NBTI.

References

1. J. H. Stathis and S. Zafar, *Microelectronics Reliab.* **46**, 270 (2006).
2. V. Huard, M. Denais, C. Parthasarathy, *Microelectronics Reliab.* **46**, 1 (2006).
3. D. K. Schroder, *Microelectronics Reliab.* **47**, 841 (2007).
4. B. Kaczer, R. Degraeve, V. Arkipov, N. Collaert, G. Groeseneken, M. Goodwin, as discussed at SISC, San Diego, CA, 2006.
5. B. Kaczer, V. Arkipov, R. Degraeve, N. Collaert, G. Groeseneken, and M. Goodwin, *Proc. Int. Reliab. Phys. Symp.*, 381 (2005); *Appl. Phys. Lett.* **86**, 143506 (2005).
6. T. Grasser, B. Kaczer, P. Hehenberger, W. Goes, R. O'Connor, H. Reisinger, W. Gustin, and C. Schlunder, *Int. Electron Devices Meeting Tech. Dig.*, 801 (2007).
7. A. Kerber, K. Maitra, A. Majumdar, M. Hargrove, R. J. Carter, and E. A. Cartier, *IEEE T. Electron Dev.* **55**, 3175 (2008).
8. M. A. Alam, *Int. Electron Devices Meeting Tech. Dig.*, 345 (2003).
9. S. V. Kumar, C. H. Kim, S. S. Sapatnekar, *IEEE/ACM International Conference on Computer-Aided Design ICCAD'06*, 493 (2006).
10. T. Grasser, B. Kaczer, W. Goes, H. Reisinger, Th. Aichinger, Ph. Hehenberger, P.-J. Wagner, F. Schanovsky, J. Franco, Ph. Roussel, and M. Nelhiebel, to be presented at *Int. Electron Devices Meeting 2010*.
11. T. Grasser, B. Kaczer, and W. Goes, *Proc. Int. Reliab. Phys. Symp.*, 28 (2008).
12. B. Kaczer, T. Grasser, J. Martin-Martinez, E. Simoen, M. Aoulaiche, Ph. J. Roussel, and G. Groeseneken, *Proc. Int. Rel. Phys. Symp.*, 55, 2009.
13. T. Grasser, B. Kaczer, W. Goes, Th. Aichinger, Ph. Hehenberger, and M. Nelhiebel, "A Two-Stage Model for Negative Bias Temperature Instability", *Proc. Int. Reliab. Phys. Symp.*, 2009.
14. T. Grasser, H. Reisinger, P.-J. Wagner, F. Schanovsky, W. Goes, and B. Kaczer, *Proc. Int. Rel. Phys. Symp.*, 16 (2010).
15. S. Rangan, N. Mielke, and E. C. C. Yeh, *Int. Electron Devices Meeting Tech. Digest*, 341 (2003).
16. G. Chen, K. Y. Chuah, M. F. Li, D. S. H. Chan, C. H. Ang, J. Z. Zheng, Y. Jin, and D. L. Kwong, *Proc. Int. Reliab. Phys. Symp.*, 196 (2003).
17. R. Fernández, B. Kaczer, A. Nackaerts, S. Demuyne, R. Rodríguez, M. Nafria, G. Groeseneken, *Int. Electron Devices Meeting Tech. Dig.* 1 (2006).
18. H. Reisinger, O. Blank, W. Heinrigs, A. Mühlhoff, W. Gustin, and C. Schlunder, *Proc. Int. Reliab. Phys. Symp.*, 448 (2006).
19. B. Kaczer, T. Grasser, Ph. J. Rouse, J. Martin-Martinez, R. O'Connor, B. J. O'Sullivan, G. Groeseneken, *Proc. Int. Reliab. Phys. Symp.*, 20 (2008).
20. E. Milotti, arXiv:physics/0204033v1.
21. H. Reisinger, T. Grasser, W. Gustin, and C. Schlunder, *Proc. Int. Reliab. Phys. Symp.*, 1 (2010).

22. V. Huard, C. Parthasarathy, C. Guerin, T. Valentin, E. Pion, M. Mammasse, N. Planes and L. Camus, *Proc. Int. Reliab. Phys. Symp*, 289 (2008).
23. T. Grasser, H. Reisinger, W. Goes, Th. Aichinger, Ph. Hehenberger, P.-J. Wagner, M. Nelhiebel, J. Franco, and B. Kaczer, *Int. Electron Devices Meeting Tech. Dig.*, 729 (2009).
24. M. Toledano-Luque, B. Kaczer, Ph. Roussel, M.J. Cho, T. Grasser, and G. Groeseneken, *presented at WoDiM 2010*.
25. M. J. Uren, M. J. Kirton, and S. Collins, *Phys. Rev.* **B37**, 8346 (1988).
26. M. J. Kirton and M. J. Uren, *Adv. Phys.***38**, 367 (1989).
27. A. Palma et al., *Phys. Rev.* **B56**, 9565 (1997).
28. B. Kaczer, T. Grasser, Ph. J. Roussel, J. Franco, R. Degraeve, L.-A. Ragnarsson, E. Simoen, G. Groeseneken, H. Reisinger, *Proc. Int. Reliab. Phys. Symp.*, 26 (2010).
29. A. Asenov, R. Balasubramaniam, A. R. Brown, J. H. Davies, *IEEE T. Electron Dev.***50**, 839 (2003).
30. A. Ghetti, C. M. Compagnoni, A. S. Spinelli, A. Visconti, *IEEE T. Electron Dev.***56**, 1746 (2009).
31. B. Kaczer, Ph. J. Roussel, T. Grasser, and G. Groeseneken, *IEEE Electron Dev. Lett.***31**, 411 (2010).
32. B. Kaczer, A. Veloso, M. Aoulaiche, and G. Groeseneken, *Microelectronic Engineering*, **86**(7-9), 1894 (2009).
33. D. Liu and J. Robertson, *Appl. Phys. Lett.* 94, 042904 (2009).
34. N. Collaert, P. Verheyen, K. De Meyer, R. Loo and M. Caymax, *IEEE T. Nanotech***1**, 190 (2002).
35. J. Franco, B. Kaczer, M. Cho, G. Eneman, G. Groeseneken, and T. Grasser, *Proc. Int. Rel. Phys. Symp.*, 1082 (2010).
36. J. Franco, B. Kaczer, G. Eneman, J. Mitard, A. Stesmans, V. Afanas'ev, T. Kauerauf, Ph. J. Roussel, M. Toledano-Luque, M. Cho, R. Degraeve, T. Grasser, L.-Å. Ragnarsson, L. Witters, J. Tseng, S. Takeoka, W.-E. Wang, T.Y. Hoffmann, and G. Groeseneken, *Int. Electron Devices Meeting 2010*.



<http://www.springer.com/978-1-4614-4077-2>

Circuit Design for Reliability

Reis, R.; Cao, Y.; Wirth, G. (Eds.)

2015, VI, 272 p. 190 illus., 132 illus. in color., Hardcover

ISBN: 978-1-4614-4077-2